Applied Catalysis B: Environmental 132–133 (2013) 282–292

Contents lists available at SciVerse ScienceDirect

Applied Catalysis B: Environmental

journal homepage: www.elsevier.com/locate/apcatb

Understanding the impact of aluminum oxide binder on Ni/HZSM-5 for phenol hydrodeoxygenation

Chen Zhao*, Yanzhe Yu, Andreas Jentys, Johannes A. Lercher**

Catalysis Research Center and Department of Chemistry, Technische Universität München, Garching 85747, Germany

ARTICLE INFO

Article history:
Received 11 September 2012
Received in revised form
25 November 2012
Accepted 26 November 2012
Available online 3 December 2012

Keywords:
Al_2O_3 binder
^{27}Al and ^{29}Si MAS NMR
EXAFS
XANES

ABSTRACT

The properties of supported Ni particles on HZMS-5 and Al_2O_3-HZSM-5 were comparably investigated by diverse characteristic techniques. Ni/Al_2O_3-HZSM-5 had at least three times higher concentrations of accessible Ni atoms (average diameter Ni^0: 8.8 nm) compared to Ni/HZSM-5 (average diameter Ni^0: 35 nm), which are consistently evidenced by TEM and XRD as well as H_2 chemisorption and IR spectra of adsorbed CO. The Ni nanoparticles interacted strongly with the binder through the interaction between NiO and Al_2O_3, explored by the combined extended X-ray absorption fine structure (EXAFS), X-ray absorption near edge structure (XANES), and H_2 temperature-programmed reduction (TPR) techniques. The Brønsted acid sites on two supports probed by IR of adsorbed pyridine were similar, but Lewis acid sites contributed by the γ-Al_2O_3 were more abundant on Al_2O_3-HZSM-5. The acid sites of the two catalysts responded differently to metal incorporation and subsequent treatments, reflecting changes in Al environments illuminated by ^{27}Al MAS NMR. In situ IR spectra of adsorbed species demonstrates that Al_2O_3-HZSM-5 has higher adsorption capacity for phenol, cyclohexanone, and cyclohexanol due to stronger adsorption of these compounds on the γ-Al_2O_3 binder.

1. Introduction

The production of high-grade liquid fuels from lignocellulosic biomass requires novel catalysts combining multiple functions [1]. Hydrodeoxygenation is a prospective technique for upgrading the crude bio-oil or lignin-derived phenolic oil to hydrocarbon liquid fuels, but requires developing active and selective catalysts. In the previous work, a series of dual functional catalysts were developed for aqueous-phase hydrodeoxygenation of phenolic oil via integrated hydrogenation, hydrolysis, and dehydration reactions [2–7]. The first-generation catalysts combined noble metal such as Pd/C and liquid acid H_3PO_4 [2,3], and the improved second-generation catalysts comprising base metal Raney Ni and solid acid Nafion/SiO_2 were also effective for such hydrodeoxygenation [4]. Recently, we developed the third-generation more durable Pd/HZSM-5 and Ni/HZSM-5 catalysts for one-pot aqueous-phase upgrading of the organic components in crude bio-oil, achieving quantitative yields of C_5–C_9 hydrocarbons [6,7]. The Ni/HZSM-5 catalyst prepared by incipient wetness impregnation was highly selective in removing oxygen from phenols, but the large Ni nanoparticles on HZSM-5 (24 nm) with a large size distribution (10 nm) at the high Ni content of the used catalyst (20 wt.%) led to a low turnover frequency (TOF) and short catalyst lifetime.

A Ni catalyst comprising 9 wt.% Ni on Al_2O_3-bound HZSM-5 with higher dispersion and narrower metal particle size distribution was synthesized in this work to compare its physicochemical properties with 9 wt.% Ni/HZSM-5. The Al_2O_3 binder increased total concentration of acid sites and in particular Lewis acid sites compared to unbound HZSM-5. It has been reported that the properties of the support, i.e., the chemical composition and type and concentration of acid sites, influence the catalytic activity of metal sites [8]. Therefore, we have investigated concentrations of metal and acid sites, the metal–support interactions, and the adsorption of reactant/intermediates on the catalysts to determine the different roles of the catalyst components on the coupled hydrogenation–dehydration reactions.

Here we report a comprehensive characterization of Ni/HZSM-5 and Ni/Al_2O_3-HZSM-5 to elucidate the different properties of the metal and acid sites, and the adsorption characteristics of these two catalysts. To directly probe the local configurations of the zeolite structural cations, ^{27}Al and ^{29}Si solid-state magic angle spinning (MAS) nuclear magnetic resonance (NMR) spectra were measured. IR spectra of adsorbed pyridine and temperature programmed desorption of NH_3 were used to quantify the acid properties of the zeolite. In addition, the treatment-induced variations in acid properties of supports and of calcined and reduced metal/zeolite

* Corresponding author. Tel.: +49 89 28912827; fax: +49 89 28913544.
** Corresponding author. Tel.: +49 89 28913540; fax: +49 89 28913544.
E-mail addresses: chenzhao@mytum.de (C. Zhao), johannes.lercher@ch.tum.de (J.A. Lercher).

0926-3373/$ – see front matter © 2012 Elsevier B.V. All rights reserved.
http://dx.doi.org/10.1016/j.apcatb.2012.11.042

catalysts were studied. The sizes, dispersions, and morphologies of the Ni particles were explored and compared using transmission electron microscopy (TEM), X-ray diffraction (XRD), H_2 chemisorption, H_2 temperature programmed reduction (H_2-TPR), IR spectra of adsorbed CO (CO-IR), and X-ray absorption spectroscopy. To compare the adsorption behavior of reactant and intermediates of phenol hydrodeoxygenation on the two catalyst samples, in situ IR spectra of adsorbed phenol, cyclohexanone, and cyclohexanol were also studied in the present work. This paper defines and interprets the physicochemical properties of Ni/HZSM-5 and Ni/Al_2O_3-HZSM-5 catalysts, while the subsequent paper explores the kinetics of the elementary steps of the phenol hydrodeoxygenation, and provides insight into the catalyst deactivation mechanisms involving the changes of metal and acid sites consequent to catalyst recovery and reuse [9].

2. Experimental

2.1. Chemicals

Catalysts were synthesized from $Ni(NO_3)_2 \cdot 6H_2O$ (Sigma–Aldrich, 99%), γ-Al_2O_3 (Degussa), HZSM-5 (Süd Chemie AG München, powder, 0.5 μm), and bound HZSM-5 (γ-Al_2O_3-HZSM-5; Süd Chemie AG München, cylindrical pellet 5 mm × 5 mm × 3 cm). The Si:Al ratio of the HZSM5 was 90. The binder was γ-Al_2O_3 comprising 21.2 wt.% of the pellets. Adsorption, catalyst preparation, and reaction studies employed phenol (Sigma–Aldrich, 99.5%), cyclohexanone (Sigma–Aldrich, 99%), cyclohexanol (Sigma–Aldrich, 99%), NH_3 (Air Liquide, >99.999%), air (Air Liquide, 20.5 vol.% O_2 and 79.5 vol.% N_2), N_2 (Air Liquide, >99.999%), He (Air Liquide, >99.996%), and H_2 (Air Liquide, >99.999%).

2.2. Catalyst preparation

Zeolite-supported Ni catalysts were synthesized by the incipient wetness impregnation method. $Ni(NO_3)_2 \cdot 6H_2O$ (2.0 g) was dissolved in H_2O (2.0 g) and the aqueous solution slowly dripped under stirring onto HZSM-5 (5.0 g) or Al_2O_3-HZSM-5 (5.0 g). After stirring for 2 h, the catalysts were dried at 373 K for 12 h, air-calcined (flow rate: 100 ml min^{-1}) at 673 K with a temperature ramp of 2 K min^{-1} for 4 h, and H_2-reduced (flow rate: 100 ml min^{-1}) at 733 K with a temperature ramp of 2 K min^{-1} for 4 h.

2.3. Catalyst characterization

2.3.1. Atomic absorption spectroscopy (AAS)

The Ni content of the catalysts was determined by atomic absorption spectroscopy (AAS) carried out with a UNICAM 939 AA-Spectrometer after solving the samples in a HF solution.

2.3.2. Specific surface area and porosity

BET surface areas, pore volumes, and pore size distributions were obtained from N_2 adsorption–desorption isotherms carried out at 77 K using a PMI automatic BET-Sorptometer. Before the measurements, the samples were outgassed at 523 K for 20 h. Surface areas and micropore and mesopore distributions were calculated according to the BET and BJH theories [10].

2.3.3. Metal dispersion (H_2 chemisorption)

Before measurement, the Ni catalysts were reduced in flowing H_2 (flow rate: 100 ml min^{-1}) at 733 K for 4 h. Subsequently the catalysts were evacuated at 588 K for 1 h and cooled to ambient temperature. A H_2 adsorption isotherm was measured at pressures from 1 kPa to 40 kPa. The sample was evacuated at ambient temperature for 1 h to remove physisorbed H_2. The quantity of H_2 chemisorbed on Ni particles was determined by extrapolating the isotherms to zero H_2 pressure, and using the difference between intercept values to estimate the dispersions of the Ni particles, assuming $H/Ni_{surf} = 1$.

2.3.4. Temperature programmed desorption of NH_3

Temperature programmed desorption (TPD) of NH_3 was performed under flow conditions in a 6-channel setup. The catalysts (ca. 100 mg) were activated in He at 473 K for 2 h at a heating rate of 5 K min^{-1} from ambient to 473 K. NH_3 was adsorbed by adding 10 vol.% NH_3 to the He carrier gas (total flow rate: 30 ml min^{-1}) at 373 K. The sample was then purged with He for 2 h to remove physisorbed molecules. For TPD of NH_3, the sample was heated in He (flow rate: 30 ml min^{-1}) at a rate of 10 K min^{-1} from 373 K to 1043 K. The species desorbing were monitored by mass spectrometry (MS Balzers QME 200) using the signal $m/e = 16$. A standard with known acid site concentration was used for quantification (Zeolite HZSM-5 with Si/Al = 45, acid site concentration = 360 μmol g^{-1}).

2.3.5. Nuclear magnetic resonance spectroscopy (NMR)

Before ^{27}Al MAS NMR measurements, the samples were hydrated over five nights in a desiccator containing a beaker with water. Then, the samples were packed into a ZrO_2 rotor and spun at 15 kHz. All spectra were measured on a Bruker AV500 spectrometer. The resonance frequency was 130.3 MHz. The spectra were the sums of 2400 sweeps with a recycle time of 250 ms. A $\pi/12$ pulse (pulse length = 1.0 μs) was applied for excitation. The chemical shifts were referenced against an external standard of solid $Al(NO_3)_3$ ($\delta = -0.54$ ppm). The ^{27}Al MAS NMR spectra were recorded using a pulse sequence including a z-filter. The pulse lengths were 3.0, 1.1, and 20.0 μs. For each row of the spectrum, 2400 scans were recorded. The recycle time was 250 ms.

The ^{29}Si MAS NMR spectra were the sums of at least 10,000 sweeps with a recycle time of 5 s. The excitation pulse had a length of 1.2 μs. The spectra were referenced against tetrakis(trimethylsilyl)silane ($\delta = -9.843$ ppm). The NMR spectra were fitted by Gaussian functions for quantitative deconvolution of overlapping peaks.

2.3.6. Infrared spectroscopy

IR spectra of adsorbed pyridine. IR spectra of adsorbed pyridine were recorded on a Perkin–Elmer 2000 spectrometer operated at a resolution of 4 cm^{-1}. The samples were prepared as self-supporting wafers (density: approximately 10 mg cm^{-2}) and activated in vacuum ($p = 10^{-6}$ mbar) for 1 h at 723 K (heating rate = 10 K min^{-1}). The activated catalyst samples were exposed to pyridine ($p_{(Py)} = 10^{-1}$ mbar) at 423 K for 0.5 h. After outgassing at 423 K for 1 h, the spectra were recorded at 423 K until no changes were observable.

IR spectra of adsorbed CO. IR spectra of adsorbed CO were measured on a Bruker VERTEX 70 spectrometer at a resolution of 4 cm^{-1}. The catalysts were activated in H_2 (partial pressure: 5 mbar) at 733 K for 1 h. Subsequently catalysts were outgassed at 733 K for 1 h ($p = 10^{-6}$ mbar) to remove H_2. After the temperature was lowered to 313 K, the catalysts were exposed to CO ($p = 0.5$ mbar) for 0.5 h. Then, the catalysts were evacuated at 313 K for 30 min to remove the physically adsorbed CO. Afterwards, the IR spectra of adsorbed CO were recorded until no further changes in the spectra were observed.

IR spectra of adsorbed phenol, cyclohexanone, and cyclohexanol. IR spectra of adsorbed phenol were measured on a Bruker VERTEX 70 spectrometer at a resolution of 4 cm^{-1}. The catalysts were activated in H_2 at 733 K for 1 h and outgassed at 733 K for 1 h ($p = 10^{-6}$ mbar) to remove hydrogen. Then, the catalyst were cooled to 313 K and exposed to phenol ($p = 0.5$ mbar) for 60 min. The IR spectra were recorded after outgassing at 313 K for 0.5 h. The

IR spectra during adsorption of cyclohexanone and cyclohexanol were recorded according to the same procedures.

2.3.7. X-ray diffraction (XRD)

The XRD patterns were recorded on a Philips X'Pert Pro System (Cu K_α, 0.154056 nm) operated at 40 kV/40 mA. Measurements were performed in the range from $2\theta = 5–70^\circ$ with a step size of 0.017°. Samples were used as a disk ($d = 2$ cm) mounted on a spinner.

2.3.8. Transmission electron microscopy (TEM)

TEM images were measured on a JEOL JEM-2010 transmission microscope operated at 120 kV. The samples for TEM examination were prepared by depositing a drop of an ultrasonicated methanol suspension of the solid material onto a carbon-coated Cu grid.

2.3.9. Scanning electron microscopy (SEM)

SEM images were obtained on a JEOL 500 SEM (accelerating voltage 25 kV). Dry samples were pulverized and gold-coated prior to scanning.

2.3.10. Temperature programmed reduction (TPR)

The TPR analysis of calcined catalysts was performed with a self-built instrument, using a 3% H_2/He mixture (flowing rate: 20 ml min^{-1}) and a heating rate of 5 K min^{-1}. The H_2O evolved during the TPR experiments was monitored by mass spectrometry (MS).

2.3.11. X-ray absorption

The X-ray absorption spectra were collected at beamline X1 at HASYLAB, DESY, Hamburg, Germany. The storage ring was operated at 4.5 GeV and typical current of 100 mA. The Si(1 1 1) double crystal monochromator was detuned to 60% of the maximum intensity to reject harmonics in the X-ray beam. The fresh samples prepared as self supporting wafers were reduced in situ with H_2 ($T = 733$ K for 1 h) followed by He treatment at 733 K for 15 min to remove the adsorbed H_2. The X-ray absorption spectra were collected at the Ni K edge (8333 eV) at 77 K for EXAFS analysis. The position of the edge was calibrated using the spectra of a simultaneously measured Ni-foil. For the EXAFS analysis, the scattering background was subtracted using third-order polynomial functions and all spectra were normalized to unity. The oscillations were weighted with k^2 and Fourier-transformed within the limits $k = 3.5–16$ Å^{-1}. The local environment of the Ni atoms in the samples were determined from the EXAFS using phase-shift and amplitude functions for Ni–O and Ni–Ni calculated assuming multiple scattering processes (FEFF Version 8.10) [11,12]. The VIPER software was used for data analysis with multi-shell fitting in the R-space. The XANES were analyzed using the XANES Dactyloscope software [13].

3. Results

3.1. Chemical compositions, textural properties, and morphologies of catalysts

The chemical compositions of the catalysts obtained in the AAS measurements are compiled in Table 1. The Ni contents were 9.2 wt.% and 9.3 wt.% on Ni/HZSM-5 and Ni/Al_2O_3-HZSM-5, respectively. The zeolite framework Si/Al ratio was 90. The Al_2O_3 content in Al_2O_3-HZSM-5 was 21.2 wt.%; it decreased to 19.3 wt.% by 9.3 wt.% Ni introduction. The N_2 adsorption–desorption isotherms of the supports were similar for HZSM-5 and Al_2O_3-HZSM-5 with BET surface areas of 417 and 381 m^2 g^{-1} (see Table 1), respectively. After Ni was introduced, the BET surface areas of the two Ni catalysts decreased by 10% compared to bare supports. Al_2O_3-HZSM-5 had a ca. 50% larger mesopore volume (0.1767 cm^3 g^{-1}) than HZSM-5 (0.1177 cm^3 g^{-1}), resulting from the interparticle mesoporosity between the Al_2O_3 binder and HZSM-5 particles. Mesopore and micropore surface areas were decreased by ca. 10% on Ni/HZSM-5; while for Ni/Al_2O_3-HZSM-5 the mesopore surface area was almost unchanged compared to the Al_2O_3-HZSM-5 precursor, but the micropore surface area was decreased by 20%. In agreement with the decreased total surface areas, the two Ni loaded catalysts had 10% smaller pore volumes than the bare supports. The mean pore diameters of the two supports and two catalysts were 3.6–3.7 nm.

SEM images of the two supports and two Ni catalysts are shown in Fig. S1. The two supports had similar morphologies: Al_2O_3-HZSM-5 had a narrow particle size distribution around 1.2–1.5 μm. By comparison, smaller particles (0.25–0.3 μm) were found in the SEM image of HZSM-5 at the average particle size of 1.5 μm, so the particle size distribution of HZSM-5 was broad. After Ni was introduced into Al_2O_3-HZSM-5, little change was observed in the particle size distribution. However, larger numbers of smaller HZSM-5 particles (0.2–0.5 μm) were formed after metal incorporation. No aggregation of support particles was observed after metal incorporation and calcination.

3.2. Characterization of configuration of catalysts

Changes in the local environment of Si and Al T_d-atoms after incorporation and reduction of Ni were characterized on unbound and bound HZSM-5 by ^{27}Al and ^{29}Si MAS NMR spectroscopy. In the ^{27}Al MAS NMR spectra (Fig. 1) overlapping signals between 54 and 65 ppm were assigned to tetrahedral (T_d) species. Resonances around at 0 ppm were assigned to extra-framework octahedral Al species. The sharp HZSM-5 peak near 0 ppm was assigned to well-ordered octahedral (O_h) Al species. A broad peak at 4.8 ppm (Al_2O_3-HZSM-5) was assigned to distorted O_h Al species. After metal incorporation, the intensity of the sharp peak at −0.8 ppm on HZSM-5 decreased from 2 mol% to 0, and the broad 4.8 ppm peak of Al_2O_3-HZSM-5 decreased from 65 mol% to 29 mol%, which indicates that the dealumination occurred during the metal incorporation.

Table 1
Element analysis and textural properties of catalysts.

	HZSM-5	Ni/HZSM-5	Al_2O_3-HZSM-5	Ni/Al_2O_3-HZSM-5
Ni (wt.%) (AAS)	–	9.2	–	9.3
Al_2O_3 binder (wt.%)	–	–	21.2	19.3
Si/Al in HZSM-5 framework	90	90	90	90
N_2 BET surface area (m^2 g^{-1})	417	383	381	351
Mesopore surface area (m^2 g^{-1})	159	148	147	159
Micropore surface area (m^2 g^{-1})	258	235	234	192
Pore volume (cm^3 g^{-1})	0.2252	0.2081	0.2741	0.2586
Mesopore volume (cm^3 g^{-1})	0.1177	0.1104	0.1767	0.1784
Micropore volume (cm^3 g^{-1})	0.1075	0.0977	0.0974	0.0802
Mean pore diameter (nm)	3.64	3.70	3.66	3.67

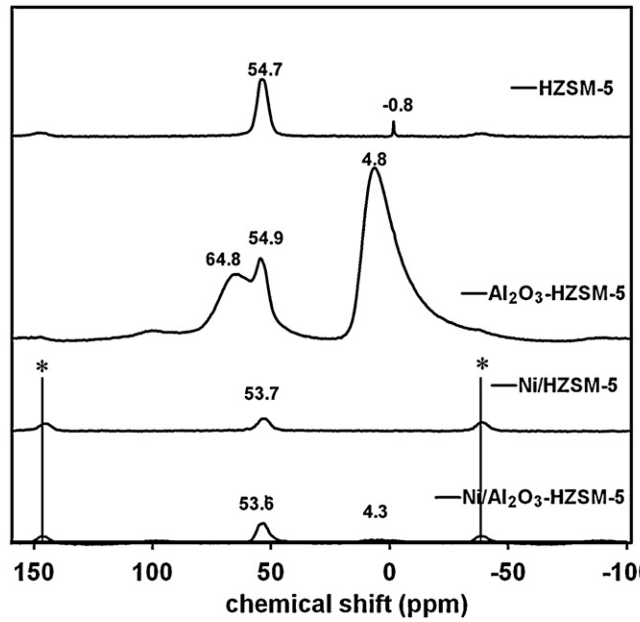

Fig. 1. [27]Al MAS NMR spectra of HZSM-5, Al_2O_3-HZSM-5, Ni/HZSM-5, and Ni/Al_2O_3-HZSM-5. The asterisks denote spinning side bands due to the quadrupolar interactions of [27]Al nuclei.

The signals from T_d Al species were assigned to framework Al atoms occupying T1 and T2 sites (54 ppm) and extra-framework T_d Al species (65 ppm) [14].

The relative areas of the different peaks are complied in Table 2. In the bare supports, 98 mol% of the Al was tetrahedrally incorporated into the framework of HZSM-5 and the remaining 2 mol% Al was in the form of O_h. For γ-Al_2O_3, it was reported that 60% O_h and 40% T_d were present in the structure [15]. After introducing Al_2O_3 binder, only 4.2 mol% of the Al was tetrahedrally incorporated into the zeolite framework of Al_2O_3-HZSM-5 and another 39.8 mol% was T_d extra-framework species. In theory, 3.5 mol% Al is calculated to be in the T_d framework of Al_2O_3-HZSM-5, when 21 wt.% Al_2O_3 is dispersed in 79 wt.% HZSM-5 (Si/Al = 90), agreeing quite well with the obtained result from [27]Al NMR spectra (4.2 mol% Al). The residual Al in the balance of Al_2O_3-HZSM-5 was O_h octahedral Al species with a fraction of 65 mol%, indicating that the added γ-Al_2O_3 is not incorporated into the framework of HZSM-5. After Ni incorporation, the intensity of the 54 ppm line (T_d Al) was drastically reduced and only very weak signals were detected from two Ni/Al_2O_3-HZSM-5 samples (Fig. 1). This suppression was a consequence of the paramagnetic character of the Ni ions, whose unpaired electrons generate a local magnetic field that strongly perturbs the resonance of the [27]Al nuclei [16]. Two weak signals from Ni/Al_2O_3-HZSM-5 at −40 and 155 ppm are spinning side bands due to the quadrupolar interactions of [27]Al nuclei [17].

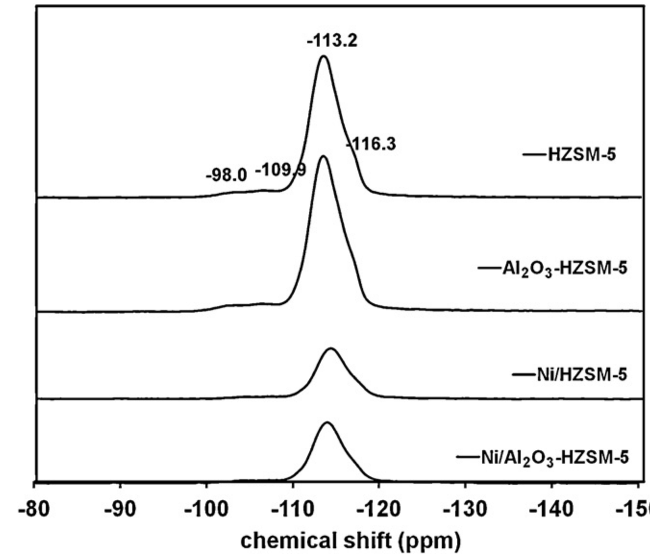

Fig. 2. [29]Si MAS NMR spectra of HZSM-5, Al_2O_3-HZSM-5, Ni/HZSM-5, and Ni/Al_2O_3-HZSM-5.

The [29]Si MAS NMR spectra of the samples are shown in Fig. 2. Fitting parameters are compiled in Table 3. According to

Table 2
Concentrations of different types of structural aluminum in supports and catalysts from deconvolution of the [27]Al MAS NMR spectra.

Catalyst	Tetrahedral (T_d-Al) (mol%)		Octahedral (O_h-Al) (mol%)
	Extra-framework (65 ppm)	Framework (54 ppm)	Extra-framework (∼0 ppm)
HZSM-5	0	98	2
Al_2O_3-HZSM-5	39.8	4.2	65
Ni/HZSM-5[a]	–	–	–
Ni/Al_2O_3-HZSM-5[a]	–	–	–

[a] The Al signal is disturbed by Ni.

Table 3
Fitting parameters of the [29]Si MAS NMR spectra of hydrated HZSM-5, Al_2O_3-HZSM-5, Ni/HZSM-5, and Ni/Al_2O_3-HZSM-5.

Si (*n*Al)	HZSM-5			Al_2O_3-HZSM-5		
	Chemical shift (ppm)	Line width (ppm)	Relative area (%)	Chemical shift (ppm)	Line width (ppm)	Relative area (%)
n = 1	−98.0	4.5	4.5	−105.8	7.8	4.8
n = 0	−109.9	15.1	24	−113.2	3.1	70
	−113.2	3.0	63	−116.2	2.2	15
	−116.3	2.0	8.5	−116.7	17.5	10
Si (*n*Al)	Ni/HZSM-5			Ni/Al_2O_3-HZSM-5		
	Chemical shift (ppm)	Line width (ppm)	Relative area (%)	Chemical shift (ppm)	Line width (ppm)	Relative area (%)
n = 1	−102.1	3.2	4.3	−102.1	2.9	4.0
n = 0	−112.9	9.0	13	−112.9	9.0	13
	−114.0	3.2	74	−114.0	3.2	75
	−117.0	2.1	8.7	−117.1	2.1	8.0

Table 4
Acid concentrations calculated from Py-IR and NH_3-TPD.

Catalyst	Conc. of BAS ($mmol\,g^{-1}$) Py-IR	Conc. of LAS ($mmol\,g^{-1}$) Py-IR	Conc. of total acid sites ($mmol\,g^{-1}$) NH_3-TPD
HZSM-5	0.076	0.046	0.152
Calcined Ni/HZSM-5	0.053	0.084	0.162
Reduced Ni/HZSM-5	0.070	0.021	0.094
Al_2O_3-HZSM-5	0.067	0.101	0.189
Calcined Ni/Al_2O_3-HZSM-5	0.041	0.084	0.162
Reduced Ni/Al_2O_3-HZSM-5	0.045	0.046	0.093

Löwenstein's rule, Al–O–Al linkages cannot occur in zeolite, and each Al atom must be coordinated to four Si atoms. One Si atom can be coordinated by 0, 1, 2, 3 or 4 Al atoms, identified by Si (0Al), Si (1Al), Si (2Al), Si (3Al), and Si (4Al) respectively. Four peaks assigned to Si (0Al) (−109 to −117 ppm) and Si (1Al) (−98 to −106 ppm) sites were detected from two supports (Table 3) [18]. The Si/Al ratios in the Ni/HZSM-5 and Ni/Al_2O_3-HZSM-5 catalysts were calculated to be 90 based on Löwenstein's rule, indicating no dealumination of the zeolite framework occurs during Ni incorporation and treatments.

3.3. Characterization of acid sites

The acid properties of the catalysts were characterized by IR spectra of adsorbed pyridine and TPD of NH_3. The concentrations of Brønsted acid sites (BAS) and Lewis acid sites (LAS) were determined from the integrated intensities of IR peaks at 1546–1547 cm^{-1} and 1447–1451 cm^{-1}, respectively. The BAS on both supports decreased after metal incorporation, and then increased after reduction but remained below uncalcined supports (Fig. S2). The variation in Lewis acidity was quite different between HZSM-5 and Al_2O_3-HZSM-5. The Lewis acidity of HZSM-5 increased after Ni incorporation/calcination and then decreased after Ni reduction, while for Ni/Al_2O_3-HZSM-5 the Lewis acidity decreased after both treatments.

The two supports had similar BAS concentrations, because those are associated almost exclusively with the HZSM-5 and were not altered when the Al_2O_3 binder was admixed and pellets formed. After Ni incorporation and calcination, the BAS concentrations were decreased by 0.023 $mmol\,g^{-1}$ (HZSM-5) or 0.026 $mmol\,g^{-1}$ (Al_2O_3-HZSM-5) compared to the two bare supports. Evidently, impregnation with 1.5% Ni (0.26 $mmol\,g^{-1}$) exchanged at least a part of the protons of BAS sites within HZSM-5 pores evidenced by the loss of BAS sites. After reduction, the BAS concentration of Ni/HZSM-5 recovered to 0.070 $mmol\,g^{-1}$, close to that of parent HZSM-5 (0.076 $mmol\,g^{-1}$), suggesting that almost all the Ni^0 particles had been generated by Ni^{2+} reduction from zeolite exchange sites. The BAS concentration of reduced Ni/Al_2O_3-HZSM-5 (0.045 $mmol\,g^{-1}$) was also almost identical to that of calcined Ni/Al_2O_3-HZSM-5 (0.041 $mmol\,g^{-1}$). This result is consistent with N_2 sorption data indicating 20% decreased micropore volume of Al_2O_3-HZSM-5 is due to the presence of small Ni particles in the pore.

The original LAS concentration on HZSM-5 of 0.046 $mmol\,g^{-1}$ increased after Ni incorporation and calcination to 0.084 $mmol\,g^{-1}$ attributed to the exchanged Ni cations, and then decreased by reduction to 0.021 $mmol\,g^{-1}$ due to reduction of Ni^{2+} as well as increased by zeolite dealumination. Al_2O_3-HZSM-5 had a higher LAS concentration (0.101 $mmol\,g^{-1}$) than HZSM-5 generated by the Al_2O_3 binder. For Al_2O_3-HZSM-5, the Lewis acidity decreased to 0.084 and then to 0.046 $mmol\,g^{-1}$ after the Ni incorporation and reduction. This result is in accordance with the ^{29}Si and ^{27}Al MAS NMR spectra.

The maximum NH_3 desorption rate (Fig. S3) during TPD occurred at 547–579 K, and the total acid concentrations decreased in the sequence supports > calcined Ni catalysts > reduced Ni catalysts. Table 4 summarizes the concentrations of BAS and LAS determined from NH_3-TPD and IR spectra of adsorbed pyridine. Both techniques agree well with the variation trend of total acid concentrations (Table 4), but the results from NH_3-TPD are 3–20% higher than those derived from IR spectroscopy. We tentatively attribute this is to the better accessibility of sites by the smaller ammonia molecules.

3.4. Characterization of metal sites

The properties of supported Ni particles were investigated by TEM, XRD, EXAFS, XANES, H_2-TPR, H_2 chemisorption, and IR spectra of adsorbed CO.

Typical TEM images of Ni/Al_2O_3-HZSM-5 and Ni/HZSM-5 showed the different Ni particle diameters on the two catalysts (see Fig. 3). For Ni on Al_2O_3-HZSM-5, the mean particle size was about 8.8 nm with a narrow standard deviation of 1.6 nm. Ni/HZSM-5 had a much larger metal particle size of 35 nm, with a large standard deviation of 13 nm and Ni crystallites on zeolite particle surfaces.

The XRD patterns of six samples including the two fresh supports, calcined Ni-, and reduced (air-exposed) Ni-catalysts are shown in Fig. 4. These all exhibited distinct and similar crystalline reflections of HZSM-5 at 2θ 8.0°, 8.9°, 23.1°, and 24.0°. HZSM-5 and Al_2O_3-HZSM-5 had almost the same XRD patterns, indicating that the crystalline properties of HZSM-5 in the two supports were almost identical. After Ni incorporation and calcination of Ni/HZSM-5, the new reflections of NiO (1 1 1), NiO (2 0 0), and NiO (2 2 0) appeared at 37.3°, 43.5°, and 62.9°. By comparison, these three peaks of calcined Ni/Al_2O_3-HZSM-5 were broad, indicating that according to the Scherrer equation much smaller NiO particles were formed on Al_2O_3-HZSM-5.

After reduction, Ni (1 1 1) and Ni (2 0 0) particles showed the new respective reflections at 44.6° and 51.9°, and the reflections of NiO at 37.3°, 43.5°, 62.9° were no longer detected. The diameters of reduced Ni particles calculated from the Scherrer equation (shape factor $K = 0.89$) of Ni (1 1 1) and Ni (2 0 0) were 6.5 and 7.1 nm on Ni/Al_2O_3-HZSM-5, and were 27.8 and 21.1 nm on Ni/HZSM-5, respectively. The size of the Ni^0 particles on Ni/Al_2O_3-HZSM-5 determined from the XRD pattern is consistent with the result from TEM image (8.8 nm), but the Ni^0 size from XRD on Ni/HZSM-5 was much smaller than that from TEM measurement (35 nm). This disparity is because XRD patterns count the average size of the single Ni^0 domains but TEM images capture larger Ni agglomerates significantly better than small ones.

XRD and TEM indicated that most of the Ni particles were larger than the pore size (ca. 3.7 nm) of ZSM-5 leading to Ni particles on the external surface in both catalysts. A fraction of small Ni particles on Ni/Al_2O_3-HZSM-5 could be within the micropore as judged from the analysis of TEM and XRD together with the N_2 sorption and the IR spectra of adsorbed pyridine.

The Fourier transformed k^2-weighted EXAFS measured at the Ni K-edge from the Ni catalysts after reduction in H_2 at 733 K followed by purging in He to remove the chemisorbed H_2 are shown in Fig. 5, and the results of the EXAFS analysis are compiled in Table 5.

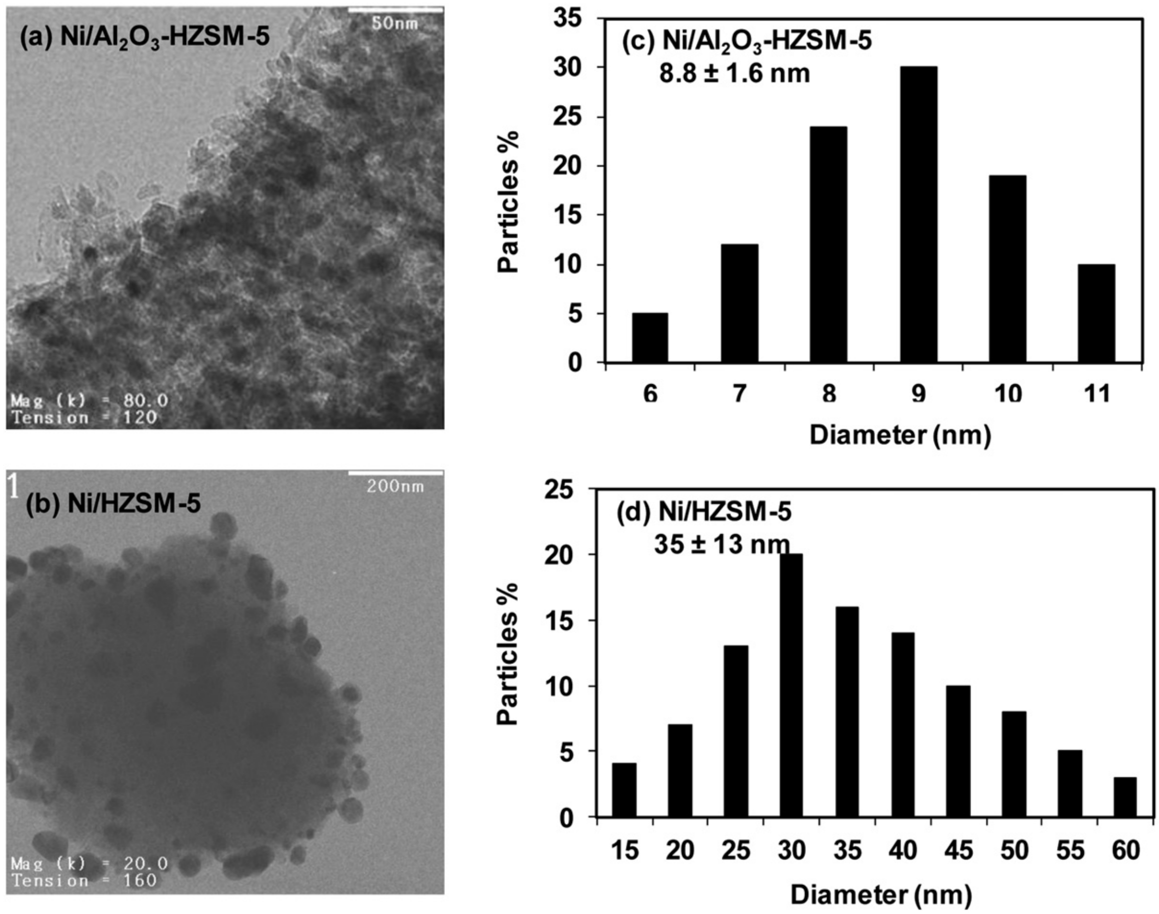

Fig. 3. TEM micrographs and particle size distributions of Ni/Al_2O_3-HZSM-5 (a and c) and Ni/HZSM-5 (b and d) (300 particles were counted for size calculation).

The coordination numbers for the Ni–Ni contributions in the first shell were 8.8 and 6.5, and the Ni–Ni interatomic distances were both 2.48 Å on Ni/HZSM-5 and Ni/Al_2O_3-HZSM-5, respectively (see Table 3). The Ni–Ni distance is in good agreement with that of fcc Ni metal (2.49 Å). The smaller Ni–Ni coordination numbers of Ni/Al_2O_3-HZSM-5 reflect the small size of Ni particles [19]. A Ni–O contribution was observed in the two zeolite supported Ni catalysts at around 1.98 Å, with coordination numbers of 0.14 and 0.61 between Ni and O for Ni/HZSM-5 and Ni/Al_2O_3-HZSM-5, respectively. The higher coordination number for the Ni–O contributions

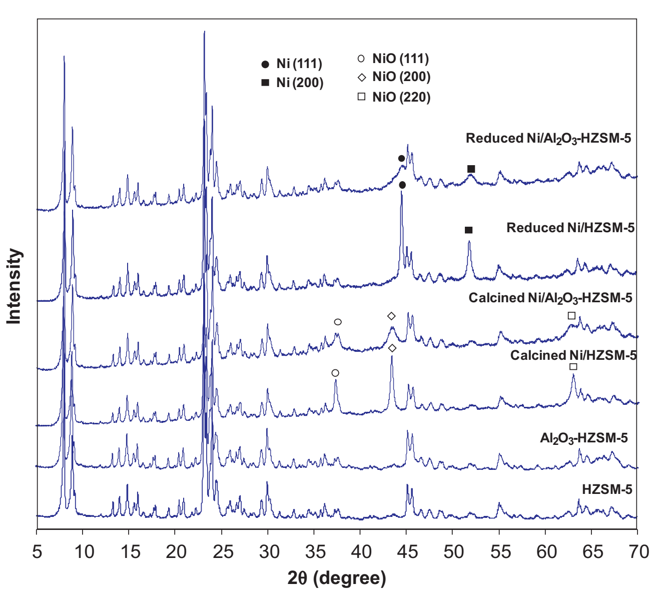

Fig. 4. XRD patterns of supports and Ni catalyst samples.

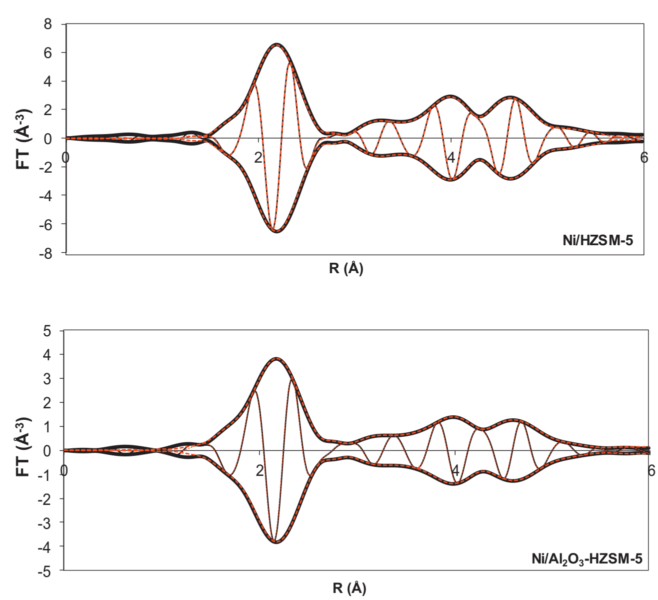

Fig. 5. Fourier transformed EXAFS of the Ni/HZSM-5 and Ni/Al_2O_3-HZSM-5 (black solid lines) and their Ni–Ni and Ni–O fitted contributions (red dotted lines) after in situ H_2 reduction at 733 K. (For interpretation of the references to color in this figure legend, the reader is referred to the web version of this article.)

Table 5
Physical characteristics of the reduced Ni particles and EXAFS and XANES fit parameters.

Catalyst	d_{XRD} (nm)	d_{TEM} (nm)	D (%)[a]	d_{chem} (nm)[b]	EXAFS analysis					XANES
					Atom pair	N	r (Å)	σ^2 (Å^2)	ΔE_0 (eV)	Reduction degree (%)
Ni foil	–	–	–	–	Ni–Ni	12	2.49	–	–	–
NiO	–	–	–	–	Ni–Ni Ni–O	12 6	2.94 2.07	–	–	–
Ni/HZSM-5	d_{111} = 27.8 d_{200} = 21.1	35 ± 13	2.5	45	Ni–Ni Ni–O	8.8 0.14	2.48 1.98	0.005 0.006	1.16 2.75	85
Ni/Al_2O_3-HZSM-5	d_{111} = 6.5 d_{200} = 7.1	8.8 ± 1.6	8.0	14	Ni–Ni Ni–O	6.5 0.61	2.48 1.98	0.007 0.002	−0.50 1.85	95

[a] Determined by H_2 chemisorption.
[b] Mean particle diameter estimated from metal dispersion as $d_{chem} = C/D$, where C is 1.17 nm for Ni.

of Ni/Al_2O_3-HZSM-5 demonstrates that the Ni oxide on Al_2O_3-HZSM-5 was incompletely reduced at 733 K. The analysis of Ni–Al coordination showed no significant backscattering and thus was not included in the fits presented here.

The XANES collected after the reduction of two Ni catalysts in H_2 flow at 733 K are compared in Fig. 6. In general, a high concentration of Al_2O_3 present on the HZSM-5 catalysts led to a lower degree of reduction of the Ni particles; hence, the Ni particles on Ni/Al_2O_3-HZSM-5 are partly oxidized. Using a linear combination of the XANES of Ni foil and NiO (Fig. 9) references for the quantitative analysis of the XANES structure, the average concentration of Ni^0 was determined to increase from 85% for the Ni/Al_2O_3-HZSM-5, and to 95% for the Ni/HZSM-5 (Table 5).

The H_2-TPR profiles of calcined Ni/HZSM-5 and Ni/Al_2O_3-HZSM-5 catalysts are shown in Fig. 7. For the Ni/HZSM-5, the reduction peaks occurred at 550, 620, and 700 K. These were assigned to the reduction of Ni oxide species that had different interactions with the support [20]. The first peak is assigned to an endothermic phase transition occurring simultaneously with a partial reduction of the NiO. The main peak at 620 K was attributed to the reduction of NiO to Ni metal. The third peak at higher temperature of 700 K was assigned to the reduction of small nickel oxide crystallites strongly interacting with the HZSM-5. For Ni/Al_2O_3-HZSM-5, one peak at 700 K belonged to the reduction of NiO and formation of Ni nanoparticles [21]. A shoulder peak centered at 900 K from the Ni/Al_2O_3-HZSM-5, taking up 15% total Ni, was attributed to the reduction of compounds between NiO and Al_2O_3 (pseudo 'spinels'), which were more refractory than NiO [22]. No spinel was detected by XRD, as the surface spinel phase lacked extended crystallinity. The less complete reduction of Ni on Al_2O_3-HZSM-5 is consistent with the higher EXAFS Ni–O coordination number that was found after reduction at 733 K. In general, changes in the maximum reduction temperature reflect the extent of interaction between the metal precursor and the support. When Ni was incorporated onto the HZSM-5 support, the weak interaction with the HZSM-5 enabled high Ni mobility as well as easy reduction so that

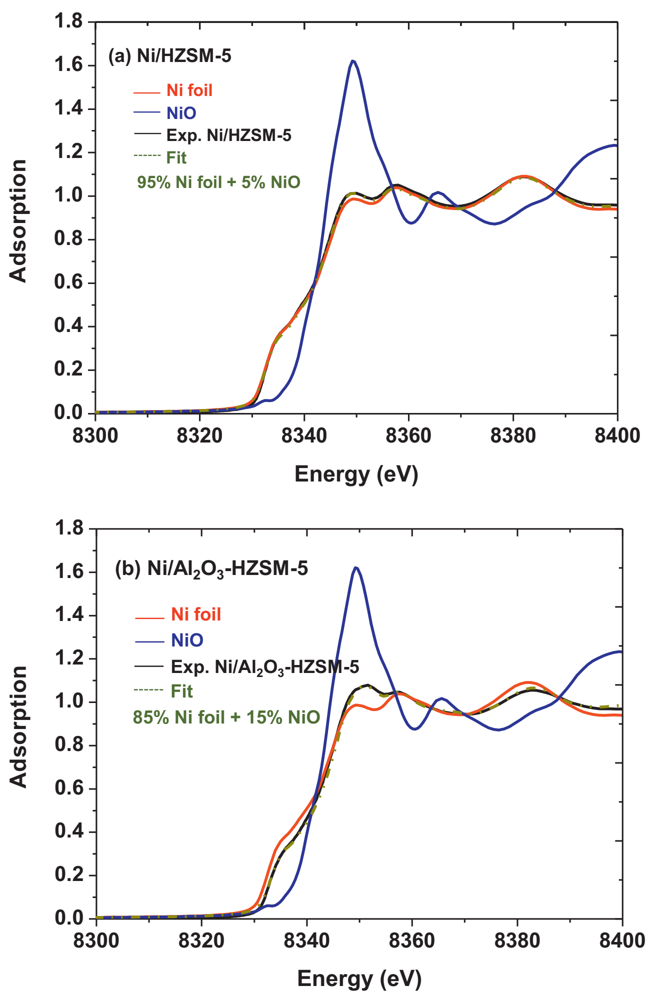

Fig. 6. XANES spectra of (a) Ni/HZSM-5 and (b) Ni/Al_2O_3-HZSM-5 after reduction in H_2 flow at 733 K.

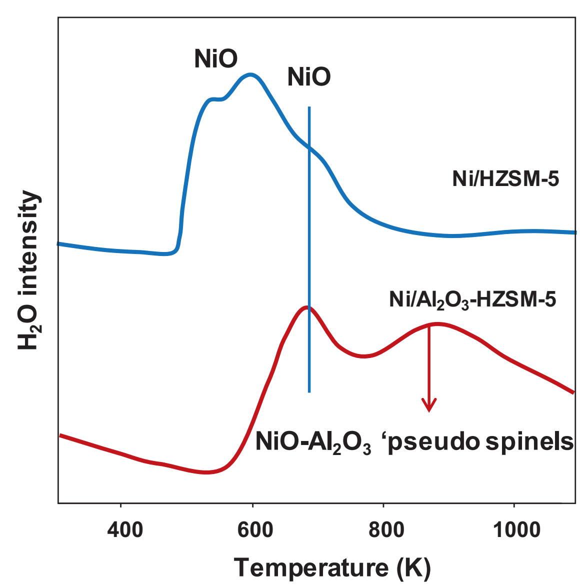

Fig. 7. H_2-TPR profiles of Ni/HZSM-5 and Ni/Al_2O_3-HZSM-5.

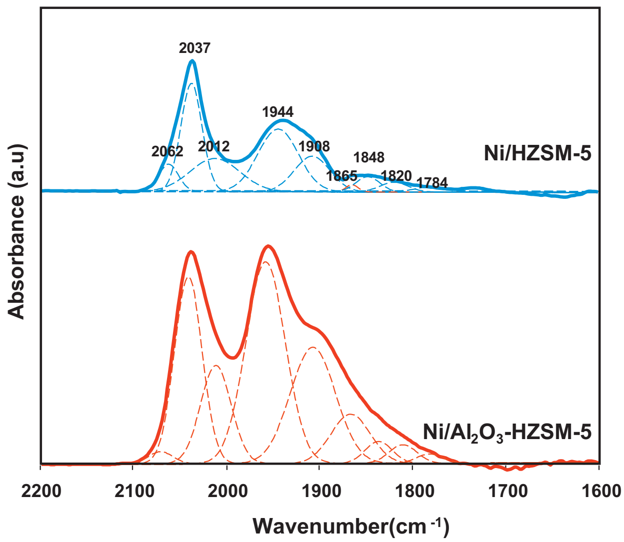

Fig. 8. IR spectra of CO adsorbed on the reduced Ni/HZSM-5 and Ni/Al_2O_3-HZSM-5; experimental data (solid line) and fitted data (dotted line).

large Ni particles (35 nm calculated by TEM) were precipitated to the external surface of the zeolite. But when Al_2O_3-HZSM-5 was used as support, much smaller Ni particles (8.8 nm calculated by TEM) including some small Ni particles lodged inside the pore system of the zeolite, and surface compounds between NiO and Al_2O_3 were formed. A much stronger interaction of metal with Al_2O_3 defect sites resulted in higher reduction temperatures of the Ni/Al_2O_3-HZSM-5.

The fraction of exposed Ni atoms was calculated from the irreversible hydrogen chemisorption at ambient conditions. With the assumption of $H/Ni_{surf.} = 1$, Ni dispersions were 8.0% and 2.5% on Ni/Al_2O_3-HZSM-5 and Ni/HZSM-5, respectively (Table 5). This result indicates that the active Ni surface sites on Al_2O_3-HZSM-5 were almost triple those on HZSM-5 with the identical 9 wt.% Ni loading. The Ni particle sizes calculated from dispersion ($d_{chem} = 1.17/D$) were 45 and 14 nm for Ni/HZSM-5 and Ni/Al_2O_3-HZSM-5 catalysts (Table 5), respectively [23]. As Ni particles for Ni/Al_2O_3-HZSM-5 were not completely reduced at 723 K, the calculated dispersion from H_2 chemisorption was lower than the true value, and therefore, the obtained d_{chem} was larger than d_{TEM} and d_{XRD}.

The accessible Ni particles on supported catalysts can also be determined from the IR spectra of CO adsorbed at $p = 0.5$ mbar. In the IR spectra shown in Fig. 8, the integrated CO adsorption intensity (2.0696) from Ni/Al_2O_3-HZSM-5 was almost triple that from Ni/HZSM-5 (0.7236) (Table S1) suggesting that the accessible Ni adsorption sites on the Ni/Al_2O_3-HZSM-5 surface were three times those on Ni/HZSM-5 assuming the same CO adsorption stoichiometry. The IR bands at ~2010–2070 cm^{-1} were assigned to terminal "linear" CO adsorption on individual Ni (1 1 1) atoms. The bands at ~1930–1950 cm^{-1} and ~1887–1910 cm^{-1} originated from molecular CO bridged across two and three Ni atoms, respectively [24]. Generally, the integrated IR intensity ratios of linear to bridge adsorbed CO (L/B) increases as Ni particle sizes decrease, because linear CO bonds preferably on low coordination sites more abundant at small particle surfaces [25]. But L/B ratio is also related to particle morphology that can vary for reasons beyond size [26]. The same sized particles with smoother surfaces (lower concentration of defect sites) yield smaller L/B ratio. In the present study, the significant decreased L/B ratio of Ni/Al_2O_3-HZSM-5 (0.512) relative to Ni/HZSM-5 (0.957) (Table 4) cannot be related to particle size as confirmed by both TEM and XRD results (see Figs. 3 and 4). Therefore, the significant decrease of the L/B ratio for Ni/Al_2O_3-HZSM-5 is supposed to be related to morphological difference, indicating that Ni/Al_2O_3-HZSM-5 has a higher concentration of close packed plane or much smoother Ni particle surface than Ni/HZSM-5.

3.5. IR spectra of adsorbed phenol, cyclohexanone, and cyclohexanol on catalysts

As phenol, cyclohexanone, and cyclohexanol are important reactant and intermediates involved into the phenol

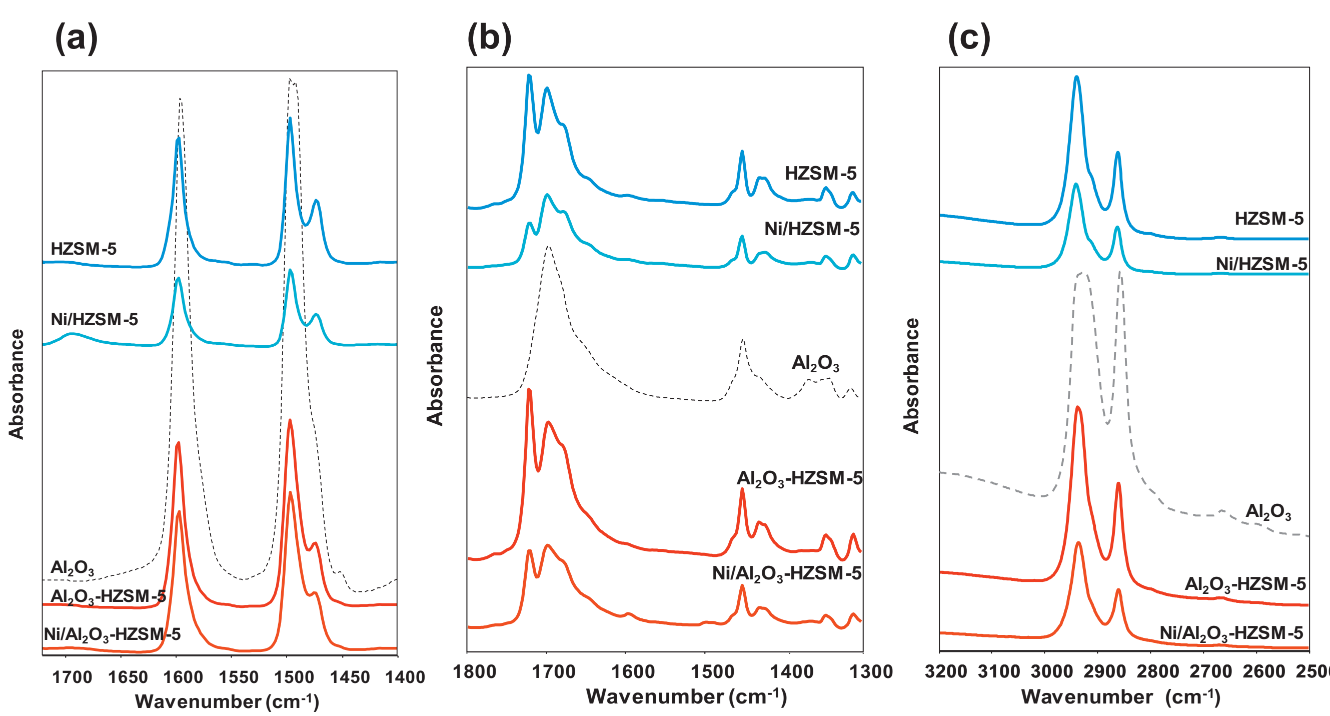

Fig. 9. IR spectra of adsorbed (a) phenol, (b) cyclohexanone, and (c) cyclohexanol on HZSM-5, Ni/HZSM-5, Al_2O_3-HZSM-5, and Ni/Al_2O_3-HZSM-5 at 313 K in the gas phase ($p = 0.5$ mbar).

Table 6
Adsorption relative capacities for phenol, cyclohexanone, cyclohexanol on supports, catalysts, and γ-Al_2O_3.

Adsorbent	IR absorbance intensities normalized to HZSM-5				
	HZSM-5	Ni/HZSM-5	Al_2O_3-HZSM-5	Ni/Al_2O_3-HZSM-5	γ-Al_2O_3
Phenol	1.00	0.55	1.36	1.21	5.27
Cyclohexanone	1.00	0.53	1.68	0.96	2.37
Cyclohexanol	1.00	0.53	1.30	0.68	2.65

hydrodeoxygenation, the in situ IR spectra of adsorbed phenol, cyclohexanone, and cyclohexanol on bare supports and on supported Ni catalysts were measured at 313 K in the presence of 5 mbar of the adsorbents (Fig. 9a–c). The ratio of integrated phenol adsorption intensities at 1597 cm^{-1} of HZSM-5 to Al_2O_3-HZSM-5 was 1:1.36 (see Table 6) showing that the phenol adsorption capacity was higher on Al_2O_3-HZSM-5 compared to HZSM-5. Ni/HZSM-5 and Ni/Al_2O_3-HZSM-5 exhibited relative phenol adsorption intensities of 0.55 and 1.21. The introduction of 20 wt.% Ni decreased the phenol adsorption capacity of HZSM-5 by 50%. In contrast, Ni/Al_2O_3-HZSM-5 retained 90% of the support adsorption capacity. Finally Ni/Al_2O_3-HZSM-5 showed two times higher phenol adsorption capacity (1.21) than Ni/HZSM-5 (0.55).

The strong cyclohexanone IR adsorption peaks at ca. 1700 cm^{-1} (Fig. 9b) document the disparity of adsorption capacities on different samples. If the integrated intensities of the 1700 cm^{-1} cyclohexanone band are normalized to the HZSM-5 sample, then relative cyclohexanone IR intensities from Al_2O_3-HZSM-5, Ni/Al_2O_3-HZSM-5, and Ni/HZSM-5 were 1.68, 0.96 and 0.53, respectively (Table 6). Cyclohexanone spectra showed similar variations as phenol adsorptions on these catalysts with cyclohexanone absorbing the IR radiation with Ni/Al_2O_3-HZSM-5 showing twice the intensity of bands of adsorbed cyclohexanone than Ni/HZSM-5 (Fig. 9b). The comparison of cyclohexanol absorption was based on the IR absorbance at 2940 cm^{-1} (Fig. 9c). Cyclohexanol adsorption capacities paralleled those of phenol and cyclohexanone among the support and catalyst samples.

4. Discussion

4.1. The comparison of Ni nanoparticles on two catalyst samples

The syntheses of the Ni/HZSM-5 and Ni/Al_2O_3-HZSM-5 catalysts were not identical. Al_2O_3-HZSM-5 was in prefabricated cylindrical pellets (5 mm × 5 mm × 3 cm) with 21.2 wt.% Al_2O_3 binder, and during the preparation it was observed that Al_2O_3-HZSM-5 absorbed the $Ni(NO_3)_2$ salt solution uniformly, and after drying was a homogeneous green color even in the internal of the pellet after being fractured. In contrast, HZSM-5 was a white powder, and after Ni^{2+} impregnation and drying at 383 K for 12 h, the catalyst was an inhomogeneous green powder with dark and light green dots, which is attributed to that some Ni^{2+} may have migrated to the surface of the bed during the static drying. The Ni solution may have been retained poorly by the relatively hydrophobic HZSM-5. Ni/HZSM-5 was paler in color than Ni/Al_2O_3-HZSM-5 after calcinations and after reduction, suggesting smaller and more uniformly distributed Ni nanoparticles on the Al_2O_3-HZSM-5 support [27].

The characterizations of metal particles by TEM, XRD, EXAFS, and XANES provided corroboration for this (Table 5). These techniques provide different profile information on Ni particle characterization, as chemisorption reflects surface reduced Ni^0, TEM counts the size of visible Ni^0 particles, XRD measures Ni domain size, XANES and EXAFS provide useful information on Ni environment. The average Ni particle size of Ni/Al_2O_3-HZSM-5 calculated from TEM (8.8 nm) was slightly larger than the size derived from XRD (6–8 nm), but the Ni particles of Ni/HZSM-5 determined by TEM (35 nm) were much larger than calculated from XRD (21–28 nm). This discrepancy is ascribed to the presence of Ni particles imaged by TEM that incorporated multiple domains. But TEM and XRD agree that Ni^0 crystallites on Ni/HZSM-5 are at least three times larger than on Ni/Al_2O_3-HZSM-5, providing a solid basis for evaluating the role of the support on the catalytic properties of Ni.

Hydrogen chemisorption quantifies the available Ni sites. The Ni dispersion from H_2 chemisorption on Ni/Al_2O_3-HZSM-5 (8.0%) was more than triple that on Ni/HZSM-5 (2.5%), which is in consistent with the IR spectra of adsorbed CO. The Ni/Al_2O_3-HZSM-5 had almost three times greater CO adsorption capacity than Ni/HZSM-5, demonstrating again that Ni nanoparticles are more highly dispersed on Al_2O_3-HZSM-5. The calculated Ni^0 particle size d_{chem} (14 nm) on Ni/Al_2O_3-HZSM-5 was much larger than d_{TEM} and d_{XRD} (9 nm), in contrast H_2 chemisorption and TEM techniques agreed that Ni particles on HZSM-5 were larger than 35 nm. This is attributed to the fact that reduction at 733 K was less complete for Ni supported on Al_2O_3-HZSM-5 than for Ni supported on HZSM-5. The discrepancy between chemisorption and TEM Ni particle sizes in the Ni/Al_2O_3-HZSM-5 catalyst is reconciled, if the extent of Ni reduction was only 70% and the true dispersion of the reduced Ni fraction was 13%.

Information on the Ni particle morphology is available from the Ni–O and Ni–Ni coordination numbers determined from the EXAFS. The Ni–Ni coordination number for Ni/HZSM-5 (8.82) is higher than that for Ni/Al_2O_3-HZSM-5 (6.49), confirming again that smaller Ni particles were dispersed on Al_2O_3-HZSM-5 [19]. The chemisorptions indicated 8% of the Ni was reduced from Ni/Al_2O_3-HZSM-5 at a surface, suggesting that the Ni–Ni coordination number equals to 11–12. The obtained smaller Ni–Ni value is attributed to numbers of small Ni particles, or unreduced Ni (having no Ni neighbors) that are too poorly ordered to contribute to the EXAFS signal. The different N (Ni–O) coordination numbers between Ni/HZSM-5 (0.14) and Ni/Al_2O_3-HZSM-5 (0.61) reflect the relatively stronger interaction of Ni^{2+} with the Al_2O_3 binder. The XANES results indicate that a high concentration of Al_2O_3 present on the HZSM-5 catalysts leads to a lower degree of reduction of the Ni particles due to the stronger interaction of metal with the support.

The H_2-TPR profiles also showed the formation of different Ni species on the two catalysts during the thermal processes. The higher 900 K temperature of H_2 reduction of Ni/Al_2O_3-HZSM-5 resulted from 'pseudo spinel' formation between NiO and Al_2O_3 surface more refractory than NiO [20]. When the reduced metal is formed from dilute and well-dispersed Ni^{2+} ions, it resisted sintering compared to metal derived from pure NiO. In addition, small metal crystallites surrounded by finely divided refractory Al_2O_3, or Al_2O_3 crystallized on the surface of Ni crystallites, prevent easy migration of metal and thereby inhibited sintering [28,29]. Using high resolution transmission electron microscopy with energy-dispersive X-ray analysis, Lamber and Schultz-Ekloff verified the existence of a nonstoichiometric $NiAl_2O_4$ phases on the surface of the Ni metal in reduced impregnated or co-precipitated NiO–Al_2O_3 catalysts [30]. It has also been proposed that Al_2O_3 was occluded within the Ni crystallites [31,32], or the phases decorating or occluding the Ni crystallites consisted of NiO–Al_2O_3 particles

[33], thereby imparting greater stability. Using the impregnation method for preparing Ni/Al_2O_3 catalysts, Wang and Lu [34] found that the Ni/Al_2O_3 (particle size: 15–20 nm) had a high reduction temperature above 1000 K. This led us to conclude that the higher metal–support interaction is deduced from the formation of $NiO–Al_2O_3$ particles, and the smaller Ni particles (ca. 8 nm) on Ni/Al_2O_3-HZSM-5 are mainly located on the external surface of HZSM-5 but not from deposition of the Ni/Al_2O_3.

4.2. The comparison of adsorption of phenol, cyclohexanone, and cyclohexanol on HZSM-5 and Al_2O_3-HZSM-5 supported Ni catalysts

The adsorbent IR spectra in Fig. 9 indicate that Al_2O_3-HZSM-5 had higher adsorption capacity by multiples of 1.3–1.7:1 for gas phase phenol, cyclohexanone, cyclohexanol than HZSM-5. After Ni incorporation, adsorption capacities decreased compared to bare supports, but Ni/Al_2O_3-HZSM-5 retained 1.3–2.2 times higher adsorption capacity than Ni/HZSM-5.

Three kinds of interactions drive adsorption of organics from the gas phase onto zeolites: (i) interaction with the zeolite lattice via dispersive van der Waals forces, (ii) direct interaction with the acid sites or cations, and (iii) intermolecular interactions of the adsorbed molecules. Since the adsorption performance was compared between different supports but the same adsorbent molecules, different intermolecular interactions are not responsible for different adsorption capacities. The zeolite type was similar, thus, the interaction of the zeolite lattice in two catalysts with the adsorbed molecules should be comparable. But, the additional 21.2 wt.% Al_2O_3 component in Al_2O_3-HZSM-5 increased the support acid density and changed its adsorption performance. Indeed, neat γ-Al_2O_3 has capacity 2.5–5.0 times higher compared to HZSM-5 for adsorption of phenol, cyclohexanone and cyclohexanol (Table 6 and Fig. 9). Evidently the Al_2O_3 binder in Al_2O_3-HZSM-5 enhanced the reactant adsorption.

The textural qualities of the two supports were quite different. The pelletized Al_2O_3-HZSM-5 had higher mesopore surface area and volume than the HZSM-5 powder (Table 1). The diffusion co-efficient of benzene and *p*-xylene in a pressed ZSM-5 pellet exceeded that in particles by eight orders of magnitude [35]; diffusion and consequent adsorption within mesopores is much faster than that in micropores. Entrance to pores and adsorption were both impeded following introduction of Ni to both HZSM-5 and Al_2O_3-HZSM-5, thus the adsorption capabilities of three reactants on the Ni based catalysts decreased.

5. Conclusion

The role of supports HZSM-5 and Al_2O_3-HZSM-5 on the catalytic properties of metal sites, acid sites, metal–support interaction, and adsorption capacities of two Ni catalysts was explored. On the metal sites, both TEM and XRD measurements support the consistent result that Ni^0 size of Ni/HZSM-5 (ca. 35 nm) is larger than that of Ni/Al_2O_3-HZSM-5 (ca. 8.8 nm), and the H_2 chemisorption data together with IR spectra from adsorbed CO indicate that Ni/Al_2O_3-HZSM-5 has almost three times more accessible Ni atoms than Ni/HZSM-5. The EXAFS and XANES results showed the Ni/Al_2O_3-HZSM-5 supported had stronger chemical interaction between metal and support. TPR found that Ni oxide on Al_2O_3-HZSM-5 was more difficult to reduce due to the formation of $NiO–Al_2O_3$ 'pseudo spinels', which prevent easy migration of metal Ni and thereby inhibited sintering.

The two supports had similar BAS concentrations, but Al_2O_3-HZSM-5 possessed higher LAS concentration due to the introduction of the γ-Al_2O_3 binder. After Ni introduction the BAS concentration of Ni/HZSM-5 exceeded that of Ni/Al_2O_3-HZSM-5 because the small Ni nanoparticles nucleated at obstructed BAS sites of Al_2O_3-HZSM-5. The LAS concentrations of both supports were diminished by Ni at least in part by dealumination during metal incorporation, calcination, and reduction.

The IR spectra of adsorbed organics showed that Al_2O_3-HZSM-5 had higher adsorption capacities for phenol, cyclohexanone, and cyclohexanol from the gas phase than HZSM-5. The γ-Al_2O_3 binder alone showed 2.5–5.0 times higher capacity for these substances compared to HZSM-5. The pore entry and surface adsorption steps were impeded by Ni in both HZSM-5 and Al_2O_3-HZSM-5, so the adsorption capacities for all three organics were decreased compared to two bare supports. The mesopore adsorption in Ni/Al_2O_3-HZSM-5 was only slightly decreased by Ni incorporation and the Ni/Al_2O_3-HZSM-5 catalysts retained higher adsorption capability than Ni/HZSM-5.

Acknowledgements

This work was supported by the Technische Universität München in the framework of the European Graduate School for Sustainable Energy. The authors thank H. Shi for the TEM, X. Hecht for BET, and M. Neukamm for AAS measurements. We also thank HASYLAB, Hamburg, Germany for providing beam time to measure the EXAFS and XANES experiments.

Appendix A. Supplementary data

Supplementary data associated with this article can be found, in the online version, at http://dx.doi.org/10.1016/j.apcatb.2012.11.042.

References

[1] A. Corma, S. Iborra, A. Velty, Chemical Reviews 107 (2007) 2411.
[2] C. Zhao, Y. Kou, A.A. Lemonidou, X.B. Li, J.A. Lercher, Angewandte Chemie International Edition 48 (2009) 3987.
[3] N. Yan, C. Zhao, P.J. Dyson, C. Wang, L. Liu, Y. Kou, ChemSusChem 1 (2008) 626.
[4] C. Zhao, Y. Kou, A.A. Lemonidou, X.B. Li, J.A. Lercher, Chemical Communications 46 (2010) 412.
[5] N. Yan, Y. Yuan, R. Dykeman, Y. Kou, P.J. Dyson, Angewandte Chemie International Edition 49 (2010) 5549.
[6] C. Zhao, D.M. Camaioni, J.A. Lercher, Journal of Catalysis 288 (2012) 92.
[7] C. Zhao, J.A. Lercher, Angewandte Chemie International Edition 51 (2012) 5935.
[8] M.F. Williams, B. Fonfé, C. Sievers, A. Abraham, J.A. van Bokhoven, A. Jentys, J.A.R. van Veen, J.A. Lercher, Journal of Catalysis 251 (2007) 485.
[9] C. Zhao, S. Kasakov, J. He, J.A. Lercher, Journal of Catalysis 296 (2012) 12.
[10] E.P. Barrett, L.G. Joyner, P.P. Halenda, Journal of the American Chemical Society 73 (1951) 373.
[11] A.L. Ankudinov, J.J. Rehr, Physical Review B 62 (2000) 2437.
[12] A.L. Ankudinov, B. Ravel, J.J. Rehr, S.D. Conradson, Physical Review B 58 (1998) 7565.
[13] K.V. Klementiev, VIPER and XANDA for Windows, freeware; K.V. Klementiev, VIPER for Windows, freeware: http://www.desy.de/~klmn/viper.html; K.V. Klementev, Journal of Physics D: Applied Physics 34 (2001) 209.
[14] J.A. van Bokhoven, D.C. Koningsberger, P. Kunkeler, H. van Bekkum, A.P.M. Kentgens, Journal of the American Chemical Society 122 (2000) 12842.
[15] J.H. Kwak, J.Z. Hu, D.H. Kim, J. Szanyi, C.H.F. Peden, Journal of Catalysis 251 (2007) 189.
[16] P. Sohár, Nuclear Magnetic Resonance Spectroscopy, CRC Press Inc., Boca Raton, FL, 1983.
[17] P. Marturano, L. Drozdová, A. Kogelbauer, R. Prins, Journal of Catalysis 192 (2000) 236.
[18] J. Pérez-Pariente, J. Sanz, V. Fornés, A. Corma, Journal of Catalysis 124 (1990) 217.
[19] A. Jentys, L. Simon, J.A. Lercher, Journal of Physical Chemistry B 104 (2000) 9411.
[20] M.V. Twigg, J.T. Richardson, Applied Catalysis A 190 (2000) 61.
[21] B. Mile, D. Stirling, M.A. Zammit, A. Lovell, M. Webb, Journal of Catalysis 114 (1988) 217.
[22] F. Medina, P. Salgre, J.L.G. Fierro, J. Sueiras, Journal of Catalysis 142 (1993) 392.
[23] M. Choi, Z. Wu, E. Iglesia, Journal of the American Chemical Society 132 (2010) 9129.
[24] S. Derrouiche, D. Bianchi, Applied Catalysis A 313 (2006) 208.
[25] J.A. Anderson, M.T. Rodrigo, L. Daza, S. Mendioroz, Langmuir 9 (1993) 2485.
[26] D.G. Blackmond, E.I. Ko, Journal of Catalysis 96 (1985) 210.

[27] N. Yan, C.X. Xiao, Y. Kou, Coordination Chemistry Reviews 254 (2010) 1179.
[28] S.P.S. Andrew, Catalyst Handbook, Springer, New York, 1970, p. 25.
[29] L.E. Alzamora, J.R.H. Ross, E.C. Kruissink, L.L. van Reijen, Journal of the Chemical Society, Faraday Transactions I 77 (1981) 665.
[30] R. Lamber, G. Schultz-Ekloff, Journal of Catalysis 146 (1994) 601.
[31] C.J. Wright, C.G. Windsor, D.C. Puxley, Journal of Catalysis 78 (1982) 257.
[32] P.C. Puxley, I.J. Kitchener, C. Komodromos, N.D. Parkyns, in: G. Poncelet, P. Grange, P. Jacobs (Eds.), Preparation of Catalysts III, Elsevier, Amsterdam, 1983, p. 237.
[33] J. Zielinski, Journal of Molecular Catalysis 83 (1993) 197.
[34] S. Wang, G.Q. Lu, Applied Catalysis A: General 169 (1998) 271.
[35] R. Kolvenbach, N. Al-Yassir, S.S. Al-Khatta, O.C. Gobin, J.H. Ahn, A. Jentys, J.A. Lercher, Catalysis Today 168 (2011) 147.